# Engineered S-Scheme g-C3N4/MnO2 Heterostructures for Integrated Photo-Rechargeable Supercapacitors with Enhanced Energy Storage Performance

P. Chinnappan Santhosh*, Suresh Jayakumar*, A. V. Radhamani*

*Energy and Innovative Materials Laboratory (EIML), Department of Physics and Nanotechnology, College of Engineering and Technology, SRM Institute of Science and Technology (SRMIST), Kattankulathur, Chengalpattu, 603203, Tamilnadu, India

## Material characterisation

The crystallographic structure of the synthesized samples was examined using X-ray diffraction (XRD) on a PANalytical X'pert powder diffractometer across a 2θ range of 10º to 80º, employing Cu Kα radiation (= 1.5406 Å) as the X-ray source at ambient temperature. A SHIMADZU UV-3600 PLUS spectrometer was employed for optical absorption and bandgap estimations. Fourier-transform infrared spectroscopy (FTIR) analysis was performed in ATR mode over the 4000-400 $cm^{-1}$ range using an Alpha-T FTIR instrument (SHIMADZU IRTRACER-100) to analyze the chemical bonds present in the as-prepared samples. The chemical valence states of the elements present in the samples were investigated using X-ray photoelectron spectroscopy (XPS) using a SHIMADZU ESCA 3100 instrument equipped with a Mg Kα X radiation source. Work functions are obtained from contact potential difference (CPD) using scanning kelvin probe (SKP5050, KP technologies Ltd., UK). Field emission scanning electron microscope (FE-SEM, Thermoscientific Apreo S) and high-resolution scanning electron microscope (HRTEM, JEOL Japan, TEM 2100 plus), both integrated with energy-dispersive X-ray (EDX) spectroscopy system, were utilized to study the surface morphology of the samples. To investigate the charge carrier recombination, the Fluorolog HORIBA instrument was employed to obtain the photoluminescence spectra (PL) at 350 nm excitation wavelength.

## Electrochemical characterisation

Electrochemical measurements were carried out using a Bio-logic SP-200 workstation. Cyclic voltammetry (CV) was conducted within the potential window of 0 to 0.8 V with scan rates ranging from 10-100 mV/s. Galvanostatic charge-discharge (GCD) tests were performed within the voltage window (0.0 -0.8 V) at various current densities between 0.3 and 0.7 $mA/cm^2$. Chronoamperometry was conducted at zero bias (V=0 V) to measure the photocurrent. Electrochemical impedance spectroscopy (EIS) was carried out across the

frequency range of 100 kHz – 100 mHz, under both dark and light (1 sun). For 1 sun intensity, a class AAA solar stimulator (Newport Corporation, USA) was used. Mott-Schottky analysis was conducted in the 3-electrode configuration using a glassy carbon working electrode modified by drop-casting M and CN samples, reference electrode as Ag/AgCl, and counter electrode as platinum wire. For the analysis, 0.5 M aqueous solution of $Na_2SO_4$ was used as an electrolyte.

Each composite functioned as the working electrode, Ag/AgCl electrode as the reference, platinum wire as the counter electrode, and 6 M KOH as the electrolyte, with a voltage window of 0 – 0.5 V.

The specific capacitance is calculated from the equation (S1),

$$Specific\ capacitance\ (F/g) = \frac{I \times t}{m \times V} \qquad \text{(S1)}$$

where I, t, m, and V represent the applied current, discharge time, mass of the active material, and potential window [47].

For the symmetric device, the areal capacitance ($C_A$) was determined from the CV curve using the equation(S2) [15],

$$C_A\left(\frac{mF}{cm^2}\right) = \frac{\int idv}{A \times \upsilon \times \Delta V} \qquad \text{(S2)}$$

Where, $\int idv$ is the integral area of the CV curve, A is the effective area of the electrode, $\upsilon$ is the scan rate, $\Delta V$ is the voltage window.

For GCD curves, $C_A$ was determined using the equation (S3),

$$C_A\left(\frac{mF}{cm^2}\right) = \frac{2I \times \Delta t}{A \times \Delta V} \qquad \text{(S3)}$$

Where, $I$ is the applied current density, and $\Delta t$ is the discharge time.

The Areal energy density ($E_A$) is evaluated using the equation (S4),

$$E_A\left(\frac{\mu Wh}{cm^2}\right) = \frac{C_A \times \Delta V^2}{2 \times 3.6} \qquad \text{(S4)}$$

The Areal power density ($P_A$)is calculated by using the equation (S5),

$$P_A\left(\frac{mW}{cm^2}\right) = \frac{E_A \times 3.6}{\Delta t} \qquad \text{(S5)}$$

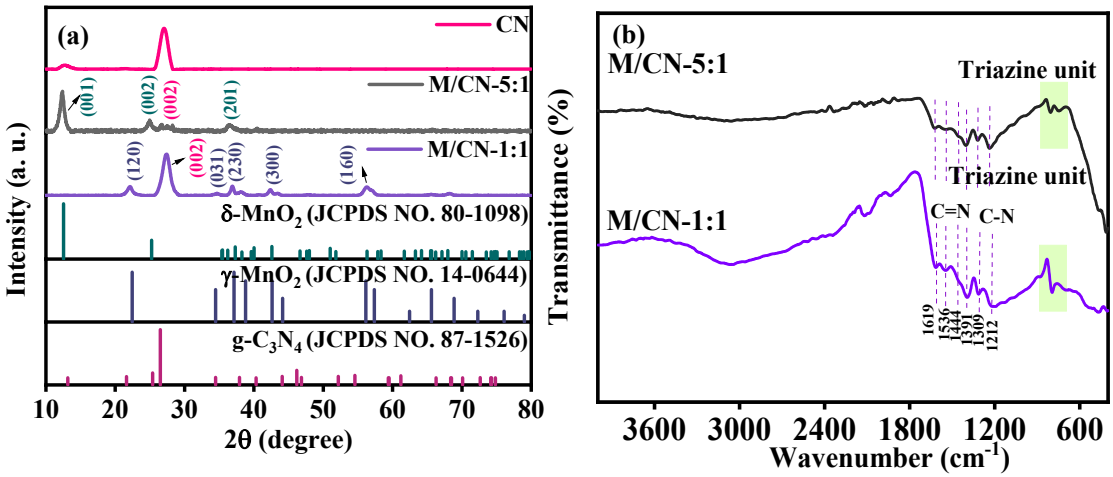


Figure. S1. (a) XRD pattern of M/CN-1:1, M/CN-5:1, and CN, (b) FTIR spectra of M/CN-1:1, M/CN-5:1, and CN respectively.

Figure. S1(a) displays the XRD peak of M/CN-1:1 positioned at 22.1°, 34.6°, 36.9°, 42.3°, and 56.2° are indexed as (120), (031), (230), (300), and (160) plane of γ-$MnO_2$ (JCPDS Card No: 00-014-0644)[1]. The high intensity peak at 22.03° attributed to the significant presence of g-$C_3N_4$ in the composite. The XRD peaks observed in M/CN-5:1 are 12.3°, 24.9° and 36.5° corresponding to the plane of (001), (002) and (201) of δ-$MnO_2$ (JCPDS Card No: 00-080-1098) respectively[2]. The low intense peak in 22.03° is due to the small amount of g-$C_3N_4$ in the composite.

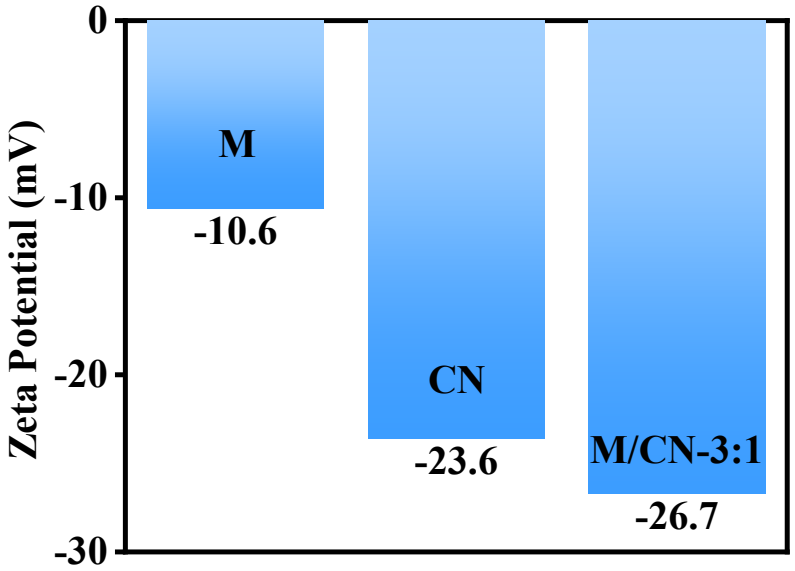

Figure. S2. Zeta potential measurements of M, CN, and M/CN-3:1 samples.

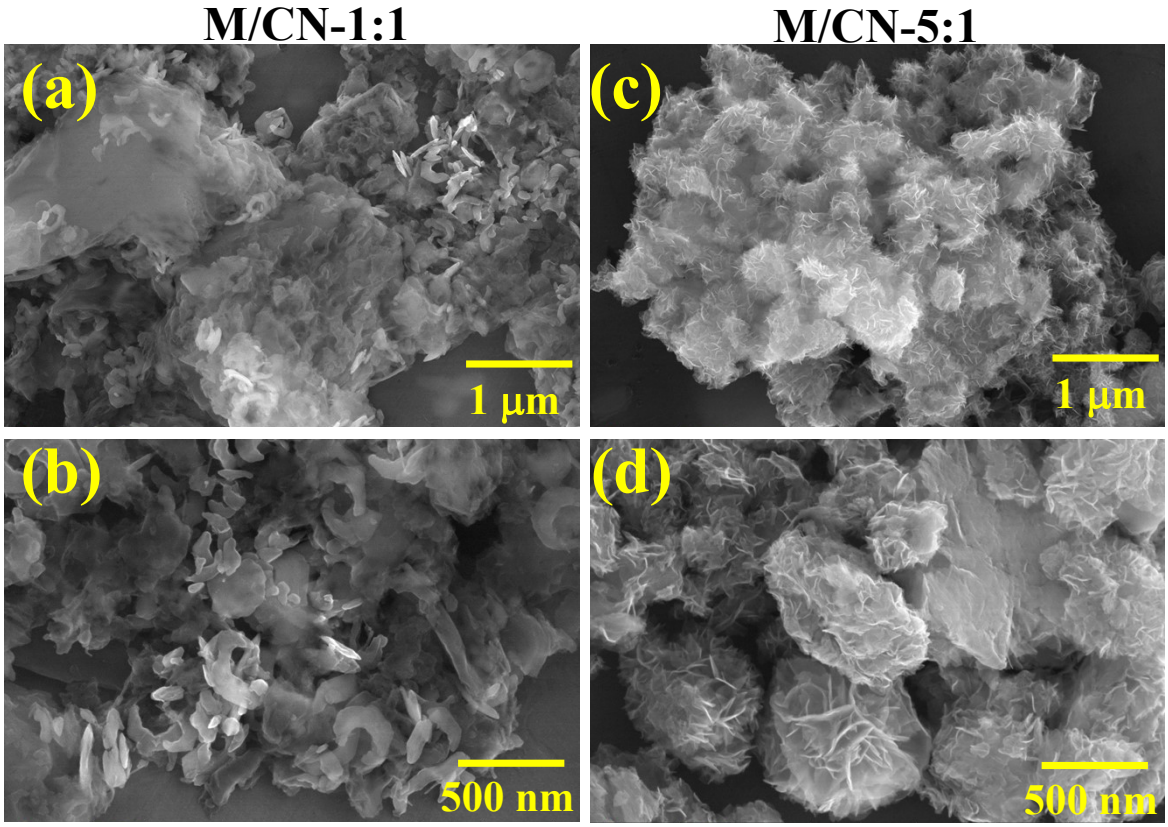


Figure. S3. (a and b) High and low magnification SEM images of M/CN-1:1 and (c and d) High and low magnification SEM images of M/CN-5:1 respectively.

The Figure. S3. (a and b) indicated the $MnO_2$ with wrinkled nanorod like morphology dispersed on the surface of g-$C_3N_4$ in M/CN-1:1, Figure. S2. (c and d) illustrate flower-like morphology by forming ultrathin nanoflakes of $MnO_2$ on the g-$C_3N_4$.

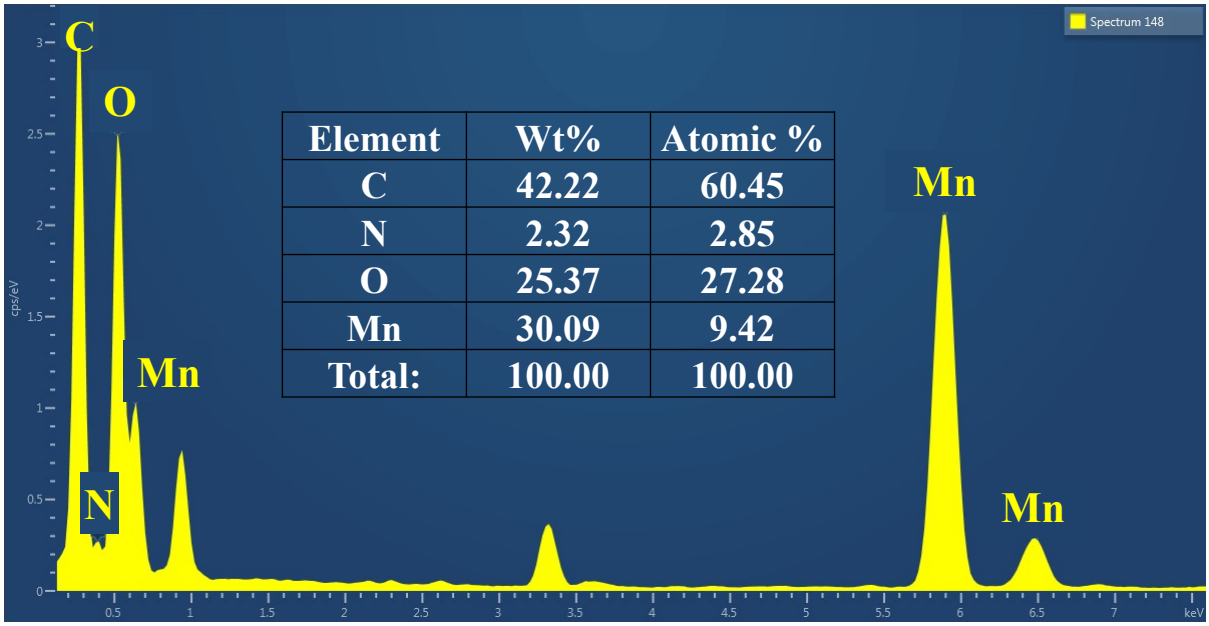


Figure. S4. EDS spectra of M/CN-3:1, inset table shows the atomic percentage of each elements present

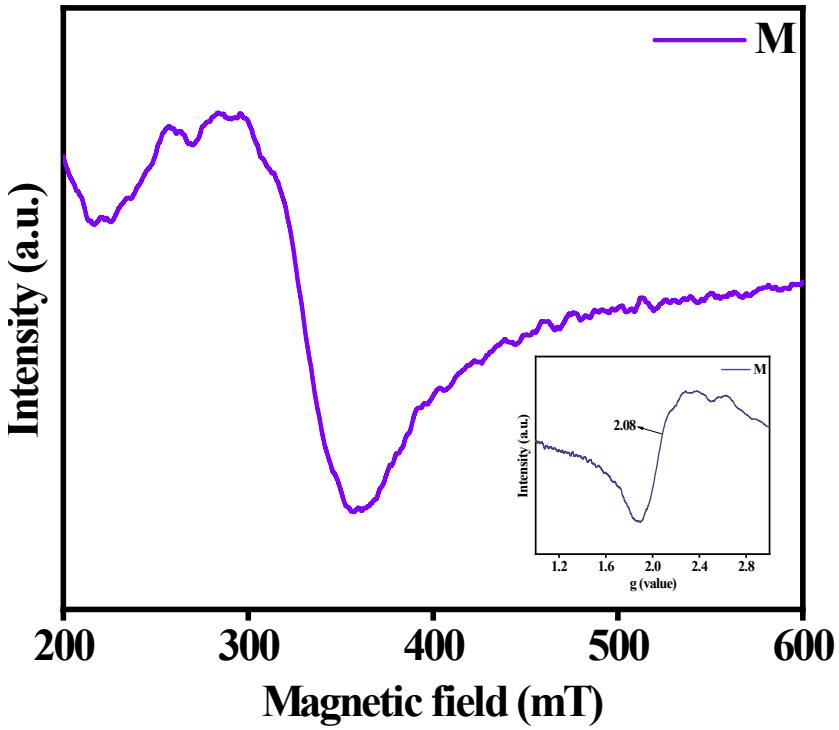


Figure. S5. ESR spectra of M sample.

Table. S1 Shows the percentage of $Mn^{3+}/Mn^{4+}$ and AOS of M/CN-3:1

| Sample name | Percentage of $Mn^{3+}$ and $Mn^{4+}$ in Mn $2p_{3/2}$ (Peak area) | | $Mn^{3+}/Mn^{4+}$ | AOS |
|---|---|---|---|---|
| | $Mn^{3+}$ | $Mn^{4+}$ | | |
| M/CN-3:1 | 69.9% | 30.1% | 2.32 | 3.61 |

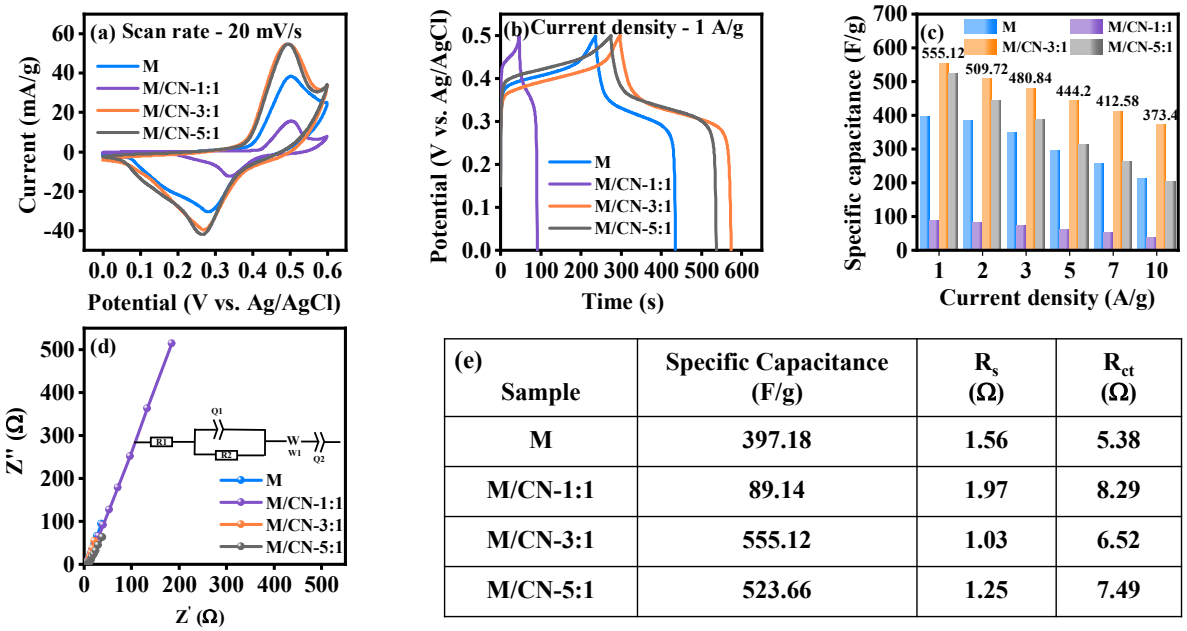


| (e) Sample | Specific Capacitance (F/g) | $R_s$ (Ω) | $R_{ct}$ (Ω) |
|---|---|---|---|
| M | 397.18 | 1.56 | 5.38 |
| M/CN-1:1 | 89.14 | 1.97 | 8.29 |
| M/CN-3:1 | 555.12 | 1.03 | 6.52 |
| M/CN-5:1 | 523.66 | 1.25 | 7.49 |

Figure. S6. (a) Comparative CV curve of M, M/CN-1:1, M/CN-3:1 and M/CN-5:1, (b) Comparative GCD curve of M, M/CN-1:1, M/CN-3:1 and M/CN-5:1, (c) specific capacitance of M, M/CN-1:1, M/CN-3:1 and M/CN-5:1, (d) Nyquist plot of M, M/CN-1:1, M/CN-3:1 and M/CN-5:1, (e) Comparison of specific capacitance, $R_s$ and $R_{ct}$ values of M, M/CN-1:1, M/CN-3:1 and M/CN-5:1

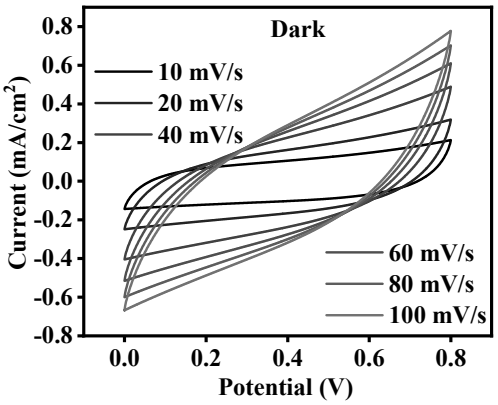

Figure. S7. CV curve at various scan rates in dark

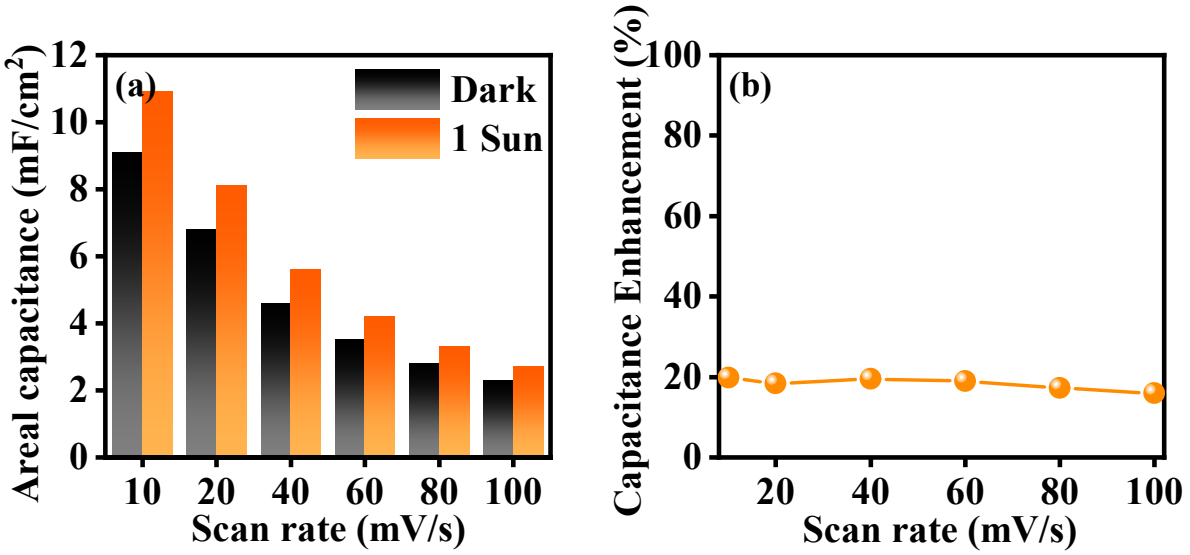


Figure. S8. (a and b) Areal capacitance at various scan rate and capacitance enhancement in light illumination of the solid-state device

Table. S2. Illustrate the fitted equivalent circuit of the solid-state device under dark and light, respectively

| Components | Dark | Light |
|---|---|---|
| Solution resistance ($R_s$) | 54.06 | 34.10 |
| Charge transfer resistance ($R_{ct}$) | 330.42 | 195.78 |
| Warberg element (W) | 272.20 | 248.39 |
| Constant phase element (Q) | 0.398 | 0.595 |
| Capacitance | 0.019 | 0.044 |

$$Z_{Re} = R_s + R_{ct} + \sigma_w \omega^{-1/2} \quad \text{(S6)}$$

$$D = \frac{R^2 T^2}{2A^2 N^2 F^4 C^2 \sigma_W^2} \quad \text{(S7)}$$

Where, $Z_{Re}$, $R_s$, $R_{ct}$, R, T, A, N, F, C, $\sigma_w$ are the real resistance, solution resistance, charge transfer resistance, ideal gas constant, temperature, electrode area, number of

electrons, faraday constant, concentration of the electrolyte and the Warburg coefficient calculated from the equation (S6), respectively.

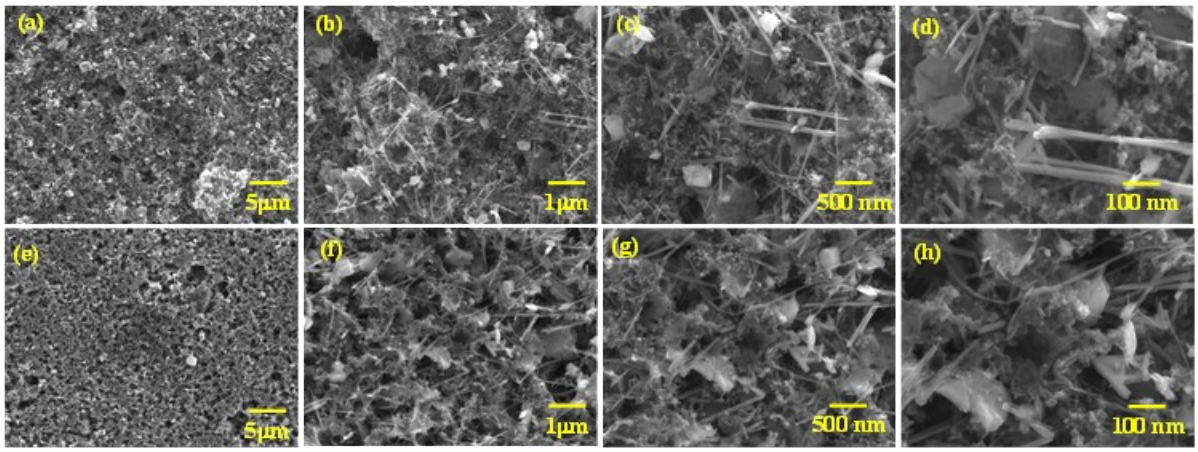


Figure. S9. (a-d) M/CN-3:1 electrode before stability, (e-h) M/CN-3:1 electrode after 600 cycles under illumination.

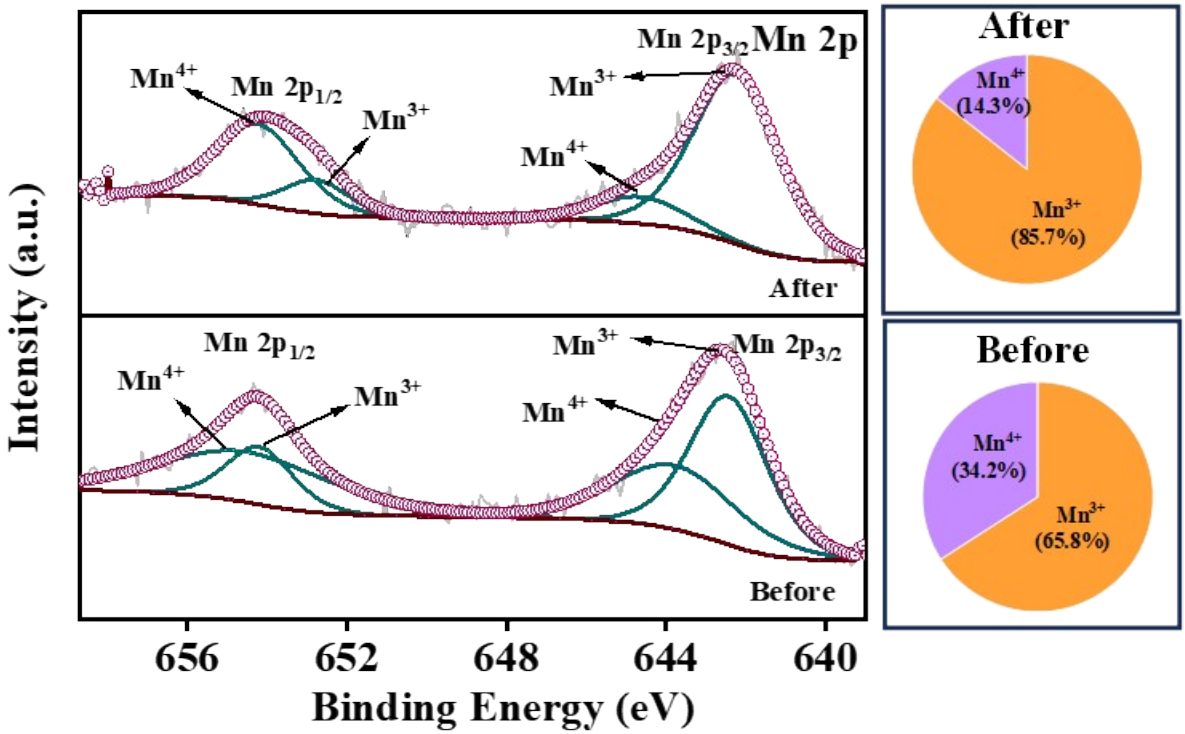


Figure. S10. High resolution spectra of Mn 2p before and after 600 cycles under illumination.

Reference:

[1] W.Y. Ko, R.S. Sitindaon, A.L. Lubis, Y.R. Yang, H.Y. Wang, S.T. Lin, K.J. Lin, Vertically-oriented zinc-doped γ-MnO2 nanowalls as high-rate anode materials for li-ion batteries, J. Energy Storage. 54 (2022). https://doi.org/10.1016/j.est.2022.105329.

[2] J. Wu, Y. Guo, W. Raza, H. Gul, G. Luo, Y. Ding, Y. Li, Y. Lv, J. Yu, L.N.U. Rehman, J. Zhao, Fast assembling MnO2-network electrode materials to achieve high performance asymmetric aqueous supercapacitors, J. Alloys Compd. 931 (2023) 167568. https://doi.org/10.1016/j.jallcom.2022.167568.

[3] M. Pourshahmir, S. Ghasemi, S.R. Hosseini, Nickel–cobalt layered double hydroxide/NiCo2S4/g-C3N4 nanohybrid for high performance asymmetric supercapacitor, Int. J. Hydrogen Energy. 48 (2023) 8127–8143. https://doi.org/10.1016/j.ijhydene.2022.11.061.

[4] G. V. Dilwale, A.C. Pawar, G. Piao, Q. Wang, Z. Said, R.K. Nimat, J. Bin In, J.M. Kim, R.N. Bulakhe, Chemical Route Synthesis of Nanohybrid Mo-V Oxide and rGO for High-Performance Hybrid Supercapacitors, Energy and Fuels. 38 (2024) 13355–13364. https://doi.org/10.1021/acs.energyfuels.4c00094.

[5] Z. Zhang, X. Ren, Y. Wang, C. Luo, G. Wang, C. Xu, H. Chen, Simple synthesis of high-performance α-NiS particles as battery-type cathode material for advanced hybrid supercapacitor application, J. Energy Storage. 116 (2025) 116091. https://doi.org/https://doi.org/10.1016/j.est.2025.116091.

[6] M.M. Mujawar, V. V Patil, V.S. Kumbhar, U.M. Patil, N.R. Chodankar, A. Al Ghaferi, M. Nakayama, J.-J. Shim, Tailored Co3O4/MnO2 heterostructure via sequential ionic layering for high performance supercapacitor applications, J. Power Sources. 642 (2025) 236980. https://doi.org/https://doi.org/10.1016/j.jpowsour.2025.236980.